Temperature-dependent conduction mechanism of NiO@Carbon@Polypyrrole nanomaterial with EMI shielding characteristics

Ujala Anwar [a,b], Numrah Sultan [a], Ghazala Yasmeen [b], Khaqan Shati [a], M. Nadeem [a,*]

[a] *Polymer Composite Group (PCG), PINSTECH, Nilore, 44000, Islamabad, Pakistan*
[b] *Institute of Chemical Sciences, Bahauddin Zakariya University, Multan, 60000, Pakistan*

A B S T R A C T

A simple hydrothermal technique and in-situ chemical oxidative polymerization of pyrrole monomer yield the functionalized NiO@C@PPy nanomaterial for electromagnetic shielding applications. The crystal structure, morphology, dielectric and electromagnetic shielding (EMI) performance in the X-band (8.2–12.4 GHz) is thoroughly studied. Impedance spectroscopy is utilized to study the electrical response of a NiO@C@PPy pellet. This study focuses on the modulations of relaxation time with frequency at different temperatures. In the NiO@C@PPy composite, a semiconductor-to-metal transition (SMT) is observed, at 328 K. The conduction mechanism of NiO@C@PPy is explained based on the carrier hopping transport model in Ni^{2+} and Ni^{3+} ions. It is evident from the activation energy value ($E_a \approx 0.32$ eV) determined from impedance, conductivity, and dielectric data that the relaxation and conduction processes correspond to the same electro-active region. Using the variable range hopping (VRH) model localization length of the carrier is calculated to be 1.56 Å. The NiO@C@PPy sample demonstrated enhanced conductivity and low dielectric values which are vital in EMI shielding applications. Consequently, the electromagnetic interference shielding effectiveness is found to be 21.9 dB of NiO@C@PPy in the X-band frequency range. This composite material is a good candidate for high frequency shielding applications.

1. Introduction

The combination of multi-phase dielectric and magnetic materials has gathered attention covering broad spectrum due to its rich fundamental physics as well as its applications in energy materials and electromagnetic shielding. Fundamentally, the co-existence of dielectric and magnetic characteristics can be tuned by modifying the synthesis parameters that can change the size, shape, and morphology of nanomaterials [1]. These characteristics can potentially optimize the scattering properties of nanocomposites to tune electromagnetic shielding (EMI) in broad frequency ranges [2]. Conventionally, the magnetic core and the dielectric shell in core-shell nanomaterials make them attractive candidates for this strategy [3]. The changed characteristics of the material result from the magnetic core, and dielectric shell, or the co-existence of both, making them good functional materials [4]. From a variety of research published on core/shell type nanomaterials, the field of electromagnetic shielding studies focus on the interaction between defect

---

chemistry, phase co-existence, and interface correlations [5].

Nickel oxide (NiO) is an intrinsically p-type semiconductor with a large band gap and high thermal and chemical stability [6]. Pure NiO is known as an electrical insulator with electrical conductivity in the range of 10^{-13} Ω^{-1} cm^{-1}. In this regard, a conducting polymer matrix with NiO core and carbon shell to tailor electric properties is carried out [7]. Due to their flexibility, superior mechanical strength, and ease of synthesis, polymer-based magnetic and dielectric composites are preferred over other conventional materials [8].

Owing to the high Curie temperature, high magnetic saturation, strong permeability, and temperature stability, nickel oxide as a core and carbon as a shell possess outstanding microwave absorption capabilities [9]. However, high density, small absorption bandwidth, and low dielectric constant restrict its potential usage [2]. Hence, the surface modification approach of coating materials (carbon & conductive polymers) on the surface of magnetic NiO particles is applied. The physical and chemical characteristics of core-shell particles are significantly different from those of their single-component counterparts. As a result, the dielectric material coating on magnetic nickel oxide particles functions as a barrier layer, enhancing the particle interface boundaries and resulting in better functionality, i.e., fewer dielectric losses [10]. The use of a dielectric layer as a shell reduces leakage by lowering the conductivity of the composites. The nanocomposite has a core/shell structure or a polymer matrix on the surface. As a result, multiphase microwave frequency-dependent materials composed of polymers with significant electric & magnetic losses may be a better selection [11].

Conventionally carbon compounds have been widely employed in microwave-absorbing materials. Carbon-based materials are the focus of research considering their low cost, high dimensional stability, low density, thermal stability, high damping, and other characteristics [12]. Carbon materials can possess good absorption qualities within a frequency domain. Fundamentally, attenuation of the incident microwave depends upon electric/dielectric loss conventionally reported as tanδ [13]. High electrical conductivity has a poor impact on surface impedance matching. Combining carbon based materials with intrinsically conducting polymers (ICPs) and magnetic materials to form carbon-coated nanomaterials is a promising technique for achieving a broad frequency spectrum for electromagnetic shielding [14]. High chemical stability of carbon materials and a considerable synergistic behavior between NiO & carbon, NiO/C composites have received a lot of attention [15]. ICPs, particularly carbon@polymer materials belong to the category of three-dimensional nanomaterial, which promotes interface polarization by expanding the interface of carbon-coated materials [16]. Electromagnetic functionalized conducting polymer based nanomaterials have gained great interest owing to their potential uses in microwave absorbent and electromagnetic shielding materials. Various researchers have published reports on electromagnetic functional nanomaterials composed of conducting polymers and related materials [17]. Because of their low chemical potential, superior electrochemical characteristics, tremendous electrical conductivity, easy manufacturing procedure, and good stability, the different ICP polypyrrole (PPy) based nanomaterials have received considerable attention [18]. Moreover, PPy-based nanomaterials have undergone substantial research for electromagnetic shielding applications. It has a broad range of conductivities (10^{-3} Scm^{-1}–100 Scm^{-1}) which depend on the monomer's functionality and substitution arrangement [19]. Polypyrrole (PPy) is a promising microwave material due to its multifunctional microwave dissipation paths, good environmental stability, tunable dielectric loss, and easy preparation method. In addition, embedding the conducting PPy with nanoparticle (NP) cores results in the electrostatic interactions between the nanoparticles and polymer matrices [20].

In this study, electromagnetic functionalized NiO@C@PPy nanomaterial is synthesized successfully using a simplistic hydrothermal method and oxidative polymerization of pyrrole monomer. To the best of our knowledge, for EMI shielding characteristics of NiO@C@PPy along with temperature-dependent conduction mechanism of electro-active regions present in the materials, no reports have been made. Impedance spectroscopy is an ideal tool for explaining the temperature-dependent conduction mechanism of the materials which is vital for understanding the origin of its EMI shielding characteristics. Conventionally, EMI shielding work focuses on attenuation of electromagnetic radiation in certain frequency domains. Temperature-dependent impedance spectroscopy is conducted to understand the role of different electroactive regions, conduction mechanisms, dielectric behavior, and ac conductivity. Using this approach, one can reveal information about the presence and movement of charge carriers. The electrical conductivity obtained at low-frequency impedance spectroscopy can be related to the EMI shielding effectiveness of the composite at higher frequencies. It's essential to note there is no straightforward or linear relationship between low-frequency impedance spectroscopy and high-frequency EMI shielding effectiveness. However, the mobility of charge carriers measured from impedance measurements and conduction mechanism within the low-frequency domain can potentially help to understand the modulation of EMI shielding performance. The correlation of electrical characteristics (high dielectric constant, tangent loss, impedance/Modulus, conductivity) with EMI shielding of the NiO@C@PPy composite can give a better understanding. A detailed insight into the electrical properties will help us correlate EMI shielding properties with electro-active regions in a broad frequency region.

2. Experimental

2.1. Materials

Ferric chloride hexahydrate (FeCl$_3$.6H$_2$O), *n*-hexane (C$_6$H$_{14}$) Pyrrole (C$_4$H$_5$N), Nickel chloride hexahydrate (NiCl$_2$.6H$_2$O), glucose (C$_6$H$_{12}$O$_6$), urea (CH$_4$N$_2$O), and ethanol (C$_2$H$_5$OH). All chemicals are of the highest purity available from Sigma-Aldrich and used as received. For solution preparation deionized (DI) water is used.

2.2. Preparation of NiO@C nanomaterials

For the synthesis of NiO@C nanomaterial, glucose (0.04 mol), NiCl$_2$.6H$_2$O (0.04 mol), and urea (0.4 mol) are mixed in 100 mL of water. The solution is then shifted to a 100 mL Teflon autoclave (Berghof High-Pressure Reactor, Model: BR-100) and kept in an oven for 12 h at 180 °C. The extracted product (NiO@C) is washed multiple times with DI water/ethanol before being dried in a vacuum oven at 50 °C for 10 h. The resulting product is calcined in a furnace at 600 °C for 4 h s. A pictorial representation of NiO@C nanomaterial is shown in Fig. 1(a) [11].

2.3. Preparation of NiO@C@PPy nanomaterial

In this procedure, blackish NiO@C powder is dispersed ultrasonically in a solution of pyrrole monomers (12 mL) and *n*-hexane (60 mL) for 1 h. Crosswise, a 12 g FeCl$_3$.6H$_2$O solution is dissolved in 100 mL DI water and cooled. The precooled oxidant solution (FeCl$_3$.6H$_2$O) is dropped into the black suspension and stirred for 24 h for the oxidative polymerization of pyrrole monomer. The resulting black precipitates (NiO@C@PPy) nanomaterials are rinsed numerous times with DI water and ethanol before being dried at 40 °C. Fig. 1(b) represents the polymerization of PPy on NiO@C nanomaterial and the formation of NiO@C@PPy [21].

The phase identification of NiO@C@PPy nanomaterial and crystallite size are measured using (ARL EQUINOX 3000). The step size 0.02 and a scanning rate 5 min^{-1} were incorporated for 15°–80° utilizing CuKα radiation. The nano-structures and morphologies are investigated by (FE-SEM) field emission scanning electron microscopy. Temperature-dependent impedance spectroscopy measurements are carried out by employing Alpha-N high-resolution dielectric analyzer (Novocontrol Technologies) and WINDETA software respectively. Shielding measurement is performed by using R&S ZNB40 VNA (10 MHz–40 GHz) Vector Network Analyzer. For analyzing EMI shielding performance, synthesized materials are ground into fine powder and mixed with paraffin evenly keeping mass ratio of 1:1 prior to molding it into a (22.5 mm × 10.1 mm) slab size.

The microstructure of the final NiO@C@PPy is as follows:

NiO (core)➡ Carbon (shell)➡ PPy (coating).

3. Results and discussion

X-ray diffraction (XRD) pattern of the NiO@C@PPy nanomaterial indicates presence of nanocrystalline NiO (see Fig. 2). A low-intensity wide diffraction peak at 24° is because of amorphous phase of C and PPy [22]. Amorphous carbon lacks long-range crystalline order and as a result, does not exhibit well-defined diffraction peaks. It is reported in the literature that amorphous carbon
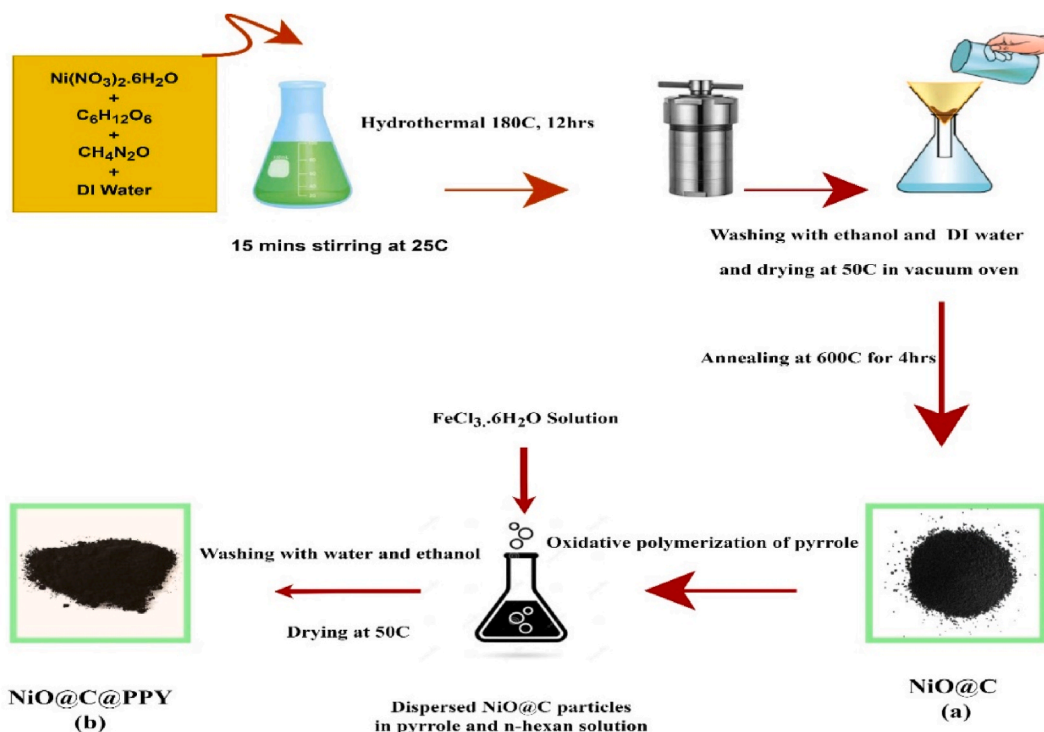

Fig. 1. (a & b) Pictorial representation to demonstrate the preparation of NiO@C(NiO core and C shell) and NiO@C@PPy (NiO core, C shell with polypyrrole coating) nanomaterial.
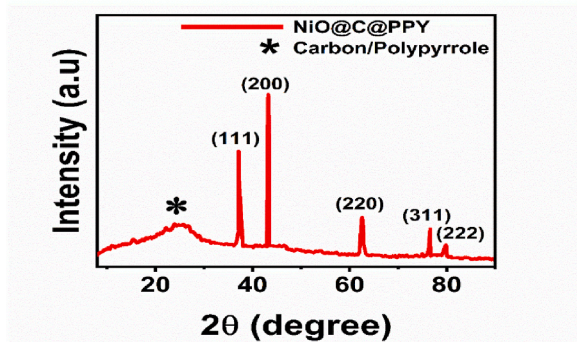
Fig. 2. XRD pattern of multiphase NiO@C@PPy nanomaterial.

shows a broad hump around 24° [23]. In the case of PPy, different researchers have reported its diffraction peak between the range of 24° to 26°. This difference can be attributed to the degree of crystallinity and doping in the polymer structure. A broad peak observed at 24°, in this case, represents amorphous PPy [24] owing to scattering caused by PPy chains at the inter-planar spacing is also reported in the literature [18,24].

The presence of the cubic nano-crystalline structure of NiO in NiO@C@PPy nanomaterial is confirmed by the peaks with 2θ values 37.05°, 43.26°, 62.76°, 75.29°, and 79.16° corresponding to the (111), (200), (220), (311) and (222) crystallographic planes, respectively. Using Scherer's equation, the average crystallite size of the NiO@C@PPy nanomaterial is determined from the highest intensity diffraction peak (200), and the determined crystallite size is around 23(±5) nm. It is reported in the literature that when the particle size is decreased to the nanoscale for particles with a size of D ≈ 24 nm antiferromagnetic materials like NiO exhibit distinct magnetic properties similar to ferromagnetism [25]. However, XRD gives information regarding crystallite size, there can be thousands of crystallites in one particle so a detailed particle size analysis can be done by employing SEM. The cubic NiO phase corresponding to the (JCPDS 47–1049) is observed [4].

FE-SEM image, as shown in Fig. 3(a and c), verified the surface morphological study of multiphase NiO@C@PPy nanomaterial. The NiO@C@PPy nanomaterial surface has a granular shape with pores between them. Fig. 3 depicts nano-crystalline NiO@C@PPy. From the SEM analysis, the morphology of NiO@C@PPy material consists of interconnected stacked nano-spheres with considerable agglomerates [26]. The particles show broad size distribution below and above 100 nm. SEM image of nano-particles performed at 100kx shows spherical particles of ≈100 nm size. Considerable agglomeration in the NiO@C@PPy material can be seen in the SEM images, therefore using ImageJ program average particle size is found out to be around 175 nm. Moreover, all the particles have sizes between 100 nm and 175 nm as the histogram depicts in Fig. 3(b).

To understand the conduction mechanism governing the multi-phase NiO@C@PPy nanomaterial, impedance spectroscopy (IS) is utilized. Fig. 4(a–c) displays the impedance plane plot for NiO@C@PPy at three different temperature zones between 183 K and 363 K. The x-intercept of the right side of the semicircle defines the total or combined resistance of the NiO@C@PPy nanomaterial, whereas on the left side, extended semicircle passes through the origin. The arrow indicates the direction from low to high frequencies. At low temperatures Fig. 4(a), the presence of only one semicircle explains the presence of one electro-active region. However, at higher temperatures, the impedance spectrum has two semicircles; the bigger semicircle in the low-frequency region and the smaller semicircle in the high-frequency region. The presence of more than one semicircle in the impedance plane plot typically indicates that two types of relaxations are present [27]. The presence of two types of relaxations can be observed by carefully examining the relaxation
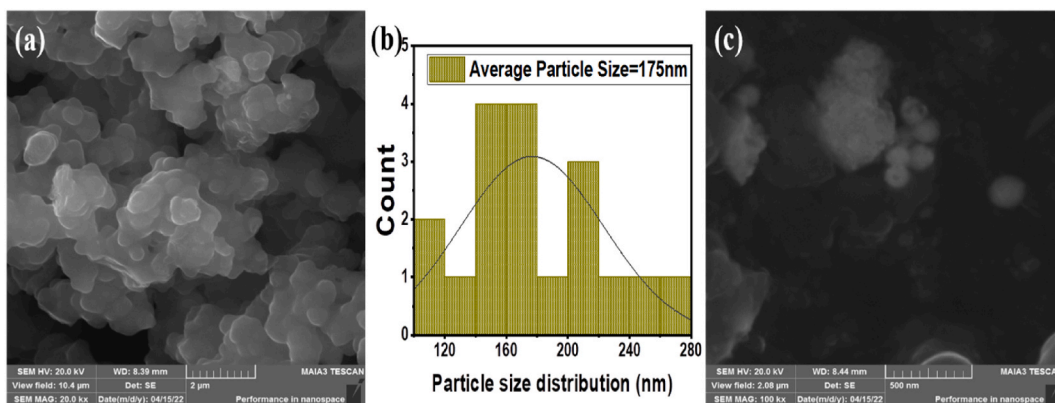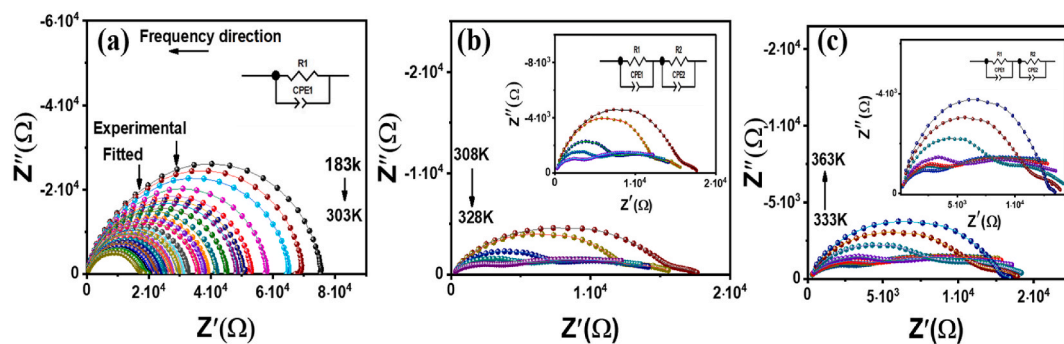

Fig. 3. (a,c) Field emission scanning electron microscopy (FE-SEM) image of multiphase NiO@C@PPy nanomaterial at 20kx and 100kx (b) histogram of average particle size distribution of NiO@C@PPy.

Fig. 4. (a–c) The plane impedance plots for NiO@C@PPy nanomaterial at three different temperature zones. Fig. 4(a) (183 K–303 K), Fig. 4(b) (308 K–328 K) & Fig. 4(c) (333 K–363 K).

time $\tau = RC$, with R being the resistance and C being the related phase's capacitance of that electro-active region. A changing trend in impedance plane plots is observed from Fig. 4(a–c); where one semicircle is shown in Fig. 4(a), which changed to two semicircles at higher temperatures in Fig. 4(b). However, in Fig. 4(c) a changing trend in the temperature dependence of the impedance plane plot is observed which will be conferred in detail in coming discussions.

For a better understanding of the conduction mechanism in the composite, software Zview is employed for matching experimental numeric data with a representative equivalent circuit to analyze corresponding impedance plane plots. Impedance plane plots acquired in the temperature zone of 183 K–303 K are fitted using a single equivalent circuit model i.e., (R_1Q_1), where R and Q are the resistance and constant phase element (CPE), respectively, as shown in the inset of Fig. 4(a). In the temperature region (308 K–328 K) & (333 K–363 K) second equivalent circuit model $(R_1Q_1)(R_2Q_2)$ is employed to fit the experimental data, as shown in the inset of Fig. 4(b and c) [28]. The suffix 1 & 2 represents two electro-active regions present in the sample. A CPE (Q) is incorporated to model the deviation of capacitance from ideal behavior, which emerged from the existence of multiple relaxation processes of similar relaxation times.

R_1Q_1 represents the equivalent circuit of carbon-coated NiO with PPy. In the temperature range of 183 K–303 K, only one circle illustrates a broad relaxation of NiO@C@PPy, however, the NiO phase dominates the conduction mechanism. A significant difference in the conduction mechanism can be seen at around 308 K because of the appearance of a second semicircle that is fitted by the addition of a second R_2Q_2 circuit. With the increase in temperature hopping carrier can diffuse from NiO through carbon coating and interacts with the electron density of PPy. The increase in interconnected channels between the polymers and oxide particles results in a strong coupling causing a reduction in the resistance for the NiO@C@PPy nanomaterial. With the increase in temperature up to 363 K, an increase in carrier mobility results in the lowering of impedance with the modulation of impedance plane plots. One can understand this changing behavior as the presence of an interface between NiO and carbon coating as well as between PPy for the decreased impedance values. The presence of depressed semicircles with temperature is due to two phases of NiO and PPy with an interface between them. The smaller semicircle arc present above 308 K specifies that more charge is transferred in the presence of a PPy polymer chain in NiO@C@PPy nanomaterial. It is interesting to note that a semiconductor-metal transition temperature (SMT) is observed where metallic behavior of the competing phases can be seen when the temperature reaches 328 K, which will be discussed in the depression angle section.

The presence of semiconductor-metal transition temperature (SMT) in NiO@C@PPy needs more clarification for a proper explanation of the origin of this transition. In this regard, we considered the defect chemistry of NiO for the onset of this transition. Fundamentally, NiO may have Ni vacancies & interstitial oxygen in NiO crystallites which may considerably affect the electrical conductivity of NiO. It is reported that proper heat treatment can modify the stoichiometry of NiO, acquiring an excess of oxygen which is balanced by the oxidation of certain Ni^{2+} to Ni^{3+} ions [25]. The additional charge on Ni^{3+} is held at the Ni vacancy in the ground state and can only be transferred through an activated hopping mechanism just like ionic diffusion. It is also reported that due to vacancy at Ni^{2+} sites, NiO develops a prototype p-type transparent conducting oxide. Ni $(3d^8 \, O \, 2p^6)$ is the electron occupancy of NiO [29]. The band structure model predicts metallic conduction because the NiO valence band has partially filled Ni 3d and O 2p orbitals. Yet, the stoichiometric NiO is insulating because the strong electron correlation in such a system prevents the transition of 3d electrons. According to the Mott-Hubbard insulator and charge-transfer insulator concepts, the band gap of NiO is thought to be formed either by

Table 1
Summary of ZView fitted parameters of the model (R_1Q_1) and $(R_1Q_1)(R_2Q_2)$ for prepared NiO@C@PPy nanomaterial at representative temperatures.

T(K)	R_1 (Ω)	R_2 (Ω)	n_1	Q_1	n_2	Q_2
183	75,165	–	0.799	2.34×10^{-10}	–	–
228	38,977	–	0.788	3.22×10^{-10}	–	–
263	26,736	–	0.774	4.61×10^{-10}	–	–
303	17,711	–	0.703	1.99×10^{-9}	–	–
328	11,810	3319	0.646	2.88×10^{-9}	0.561	2.19×10^{-6}
343	11,294	2299	0.639	5.82×10^{-9}	0.540	1.19×10^{-6}
363	11,162	2065	0.621	1.30×10^{-9}	0.539	3.59×10^{-6}

the higher metal site and O 2p site or by splitting the Ni 3d channels under strong electron correlation [30]. From the above discussion, one can infer that SMT in NiO@C@PPy occurs as a result of the defect chemistry of NiO in NiO@C@PPy.

Using an equivalent circuit model the values of resistance of the electro-active region (R_1), as given in Table 1, are used for explanation of conduction mechanism. We employed two models, Mott variable range hopping (MVRH) and small polaronic hopping (SPH) model in the temperature range of (183 K–303 K).

The MVRH model is generally expressed as $ln\,(\rho\,/\rho_a) = (T_0/T)^{1/4}$, describing the mechanism of hopping transport in a system where the carriers are localized by the random variation in potential. The sites falling within a specific range of energies are preferred for the hopping. Based on fitted parameters of the equivalent circuit, resistance (R_1) is plotted against the reciprocal of temperature using the MVRH model in the temperature range of 183 K–303 K as shown in Fig. 5(a). The localization length of the hopping carrier of NiO@C@PPy nanomaterial was calculated to be $1/\alpha = 1.56$ Å obtained from the fitting of the MVRH model [31]. Because of random fluctuations in potential at low temperatures, the charge carriers more likely jump with varying activation energies farther apart than their closest neighbor. The small polaronic hopping (SPH) model is applied by using the expression $ln\rho/T = lnA + W/kT$ in the temperature range of 183 K–303 K as shown in Fig. 5(b). The values of the obtained activation energies $E_a = 0.14$ eV also support polaronic conduction in this nanomaterial. At this temperature, many trap centers localize the charge carriers which start following the SPH conduction model by encouraging effective connections between Ni^{2+} and Ni^{3+} channels. There is a large barrier to the transportation of charge carriers since PPy is p-type. Based on fitted data parameters, it is inferred that the small polaron hopping model fitting is better than the Mott variable range-hopping model for NiO@C@PPy.

As we discussed previously, the size of the semicircle and center is affected by temperature in the NiO@C@PPy nanomaterial. The depression angle is the displacement of the experimental impedance plane plot below the real axis due to the distributed elements and heterogeneity in the system. The depression angle of all temperature-dependent impedance data is calculated using Zview software. Fig. 5(c) shows how the depression angle varies with temperature. Fig. 5(c) shows the depression angle increases with temperature and reaches the high value of 53° around SMT (328 K). After SMT, a further increase in temperature resulted in a drop in depression angle values. These findings show that there is only one peak in the values of depression angles at 328 K which is in accordance with impedance findings at semiconducting to metallic transition temperature (SMT) [32]. A continuing trend towards lowering of depression angle with the temperature can be seen. To explain such higher values of depression angles, we need to explore the fundamentals of Ni^{2+} ions in NiO, which are in the 3 d^8 state. Whereas, each Ni^{2+} atom has two well-localized 3d electrons, and the dx^2-dy^2 and dz^2 orbitals are energetically unfavorable, having a potential to deviate from symmetry. It is reported in the literature, Ni^{2+} and O_2 are stabilized by Jahn-Teller distortions by altering the highly antibonding D-state by eliminating an electron to cause decrease in the energy. As a result, the Ni–O–Ni bond is stretched more along the z-axis than the x-axis. Because of the charges and local lattice distortions, polaron formations are affected [25]. These distortions along with space charge produced at interfaces of NiO, carbon, and PPy resulted in higher depression angles around SMT.

To understand the frequency dependence of M'' and Z'' with the temperature different electro-active sites are explored in NiO@C@PPy nanomaterials. It is worth mentioning that modulus formalism offers the improvement of suppressing electrode polarization effects. Fig. 6(a–d) shows that the spectra of Z'' and M'' have a single relaxation-based response. Fig. 6(a) shows a single relaxation in the Z'' graph in the temperature range of 183 K–328 K at $\approx 10^5$ Hz. By elevating temperatures, not only single relaxation changes to two relaxations in the temperature range of 333 K–363 K, as shown in Fig. 6(b). The appearance of two relaxations is in accordance with our previous discussions in complex impedance plane plots. It is also noted that the relaxation at 10^5 Hz shifted to $\approx 10^6$ Hz. In the inset of Fig. 6(b), the relaxation period ($\tau = 1/2\pi f_{max}$) is plotted against the temperature, which is proportional to Z'' peak frequency (f_{max}) [33]. The activation energy of the NiO@C@PPy nanomaterial as calculated from the slope is 0.31 eV. Fig. 6(c) shows a single relaxation peak in the M'' graph in the temperature range of 183 K–328 K at $\approx 10^6$ Hz. It is observed that when the temperature is increased from 333 K to 363 K, the frequency of the peak is shifted from 10^6 Hz to 10^7 Hz as shown in Fig. 6(d) [6]. It is possible to figure out whether the relaxation processes are predominantly governed by the mobility of short-range or long-range charge carriers by comparing the frequency-dependent spectra of both M'' and Z''. Fig. 6(a and c), indicates that the peak frequencies of Z'' and
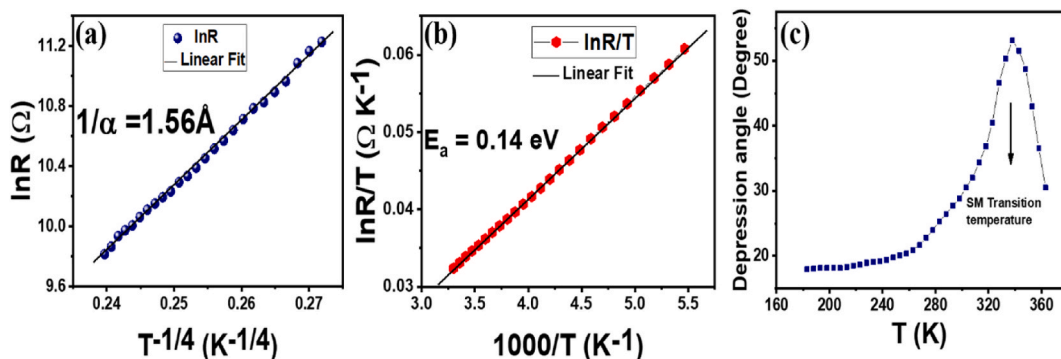

Fig. 5. Shows the variation of resistances against reciprocal of temperatures. (a) Mott variable range hopping (MVRH) model from 183 K to 303 K (b) Line in solid represent best fit for small polaron hopping (SPH) model from 183 K to 303 K (c) Shows the plot of the depression angle with a temperature for NiO@C@PPy nanomaterial.
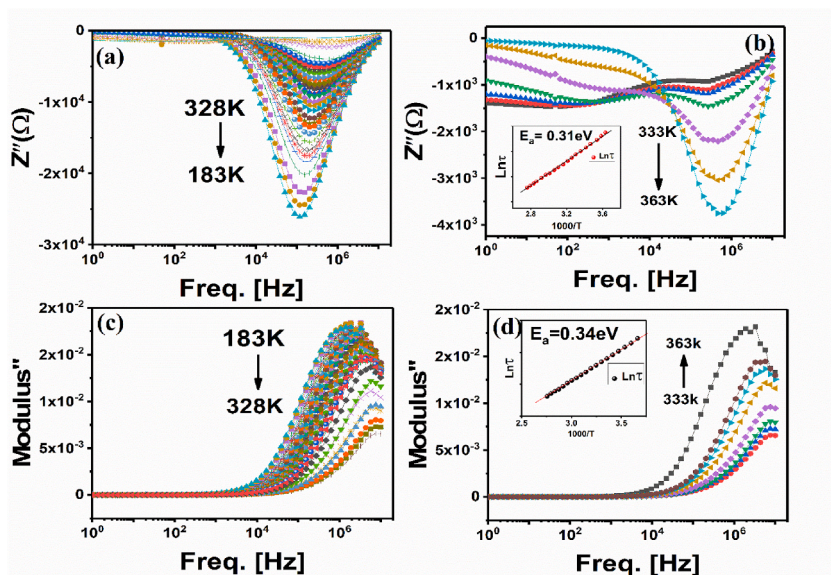
Fig. 6. (a–d) The frequency-dependent M″and Z″ at two different temperatures zone. (183 K–363 K) for NiO@C@PPy nanomaterial. (a,c) (183 K–328 K) & (b,d) (333 K–363 K).

M″ at different temperatures are apart, from where it can be inferred that the mobility is caused by the movement of short-range charge carriers. Around SMT and higher temperatures, the peak frequencies of Z″ and M″ are close in range, which shows the mobility of carriers is influenced by the movement of long-range charge carriers [34]. In the inset of Fig. 6(d), the activation energy of the nanomaterial as calculated from the slope is 0.34 eV.

Fig. 7(a) depicts the frequency-dependance of dielectric constant (real part) at (183 K–328 K) & 7(b) (328 K–363 K) temperatures. These graphs demonstrate the occurrence of multiple types of polarizations in NiO@C@PPy nanomaterials. Interfacial, atomic, electronic & dipolar polarizations are the most common types of polarizations that are reported [35]. Polaron and bipolaron are the two main types of charge carriers that are often found in polymer composites [36]. Because localized or immobilized dipoles are present at low frequencies and can migrate over long distances, this results in a high dielectric constant. The dipoles polarize at these frequencies due to enough time, which raises the dielectric constant as reflected in Fig. 7(a and b) [6]. Fig. 7(c and d) highlight the
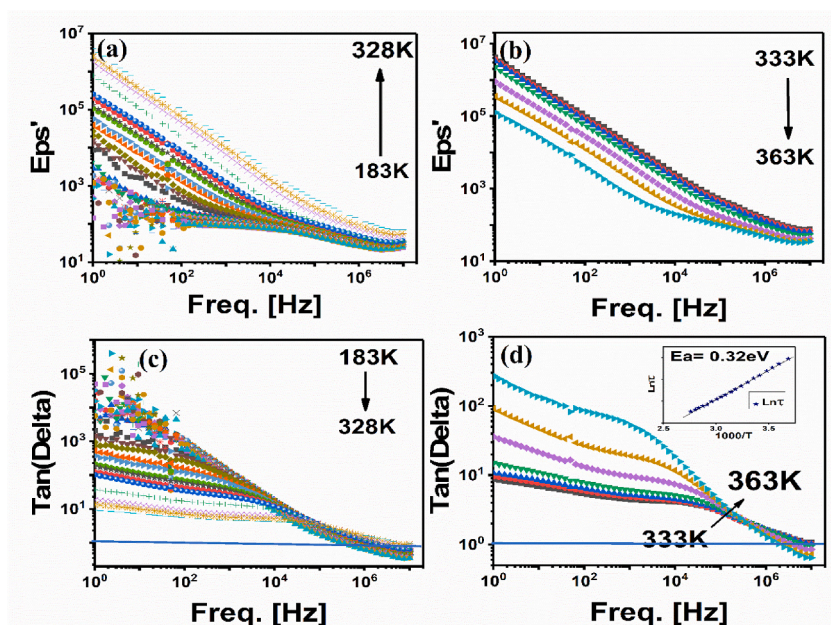

Fig. 7. Frequency-dependent dielectric constant (ε) and dielectric loss (tanδ) for multiphase NiO@C@PPy nanomaterial at two different temperature zones. (a,c) (183 K-328 K) & (b,d) (333 K–363 K). Inset in the Fig. (c) shows the relaxation time at the peak frequency.

significantly higher values of loss at low frequencies throughout the polarization process as a result of these dipoles' alignment shift (short-range migration). The relaxation process causes the dielectric constant to drop at higher frequencies. The electric field changes its direction in this frequency range before the dipoles align themselves with the field and become frequency independent, results in the lowering of the dielectric loss. Increased values of tanδ in NiO@C@PPy nanomaterials are mainly the result of significant polarization effects occurring both inside the polymer network and between the NiO components. Strong dipoles occur in the pyrrole molecule as a result of the strong polarization effect, and their arrangement and orientation help to increase the tanδ value. Fig. 7(a and b) shows that the dielectric dispersion originates in the 10^4 Hz region at SMT and shifts to 10^5 Hz at 328 K, matching the relaxation frequency of the electro-active region. These results are inconsistent with impedance results where a decrease in impedance values with temperature results in higher dielectric constant values for the interface present between NiO@C@PPy nanomaterial. It is suggested that extended defects, which can mediate the distant interactions may be the cause of SMT and dielectric modulation. According to dielectric investigations, the structural inhomogeneity is the underlying cause for the interfacial phenomena at low frequencies and the connection of Ni^{2+} ions is responsible for orientation polarization at high frequencies [37]. Due to the strong interfacial polarization, the dielectric permittivity is high. The dielectric constant gradually drops at higher frequencies, as reflected in Fig. 7(a and b). Higher values of the dielectric constant are also a result of the formation of a connected network that emerges from the heterogeneity of the NiO@C@PPy nanomaterial. Furthermore, at high temperatures, an anomalous decrease in dielectric constant and an increase in tanδ occurs with lowering frequencies. It is worth noting that the observed characteristics for the frequency dependence of dielectric constant and dielectric loss (tan δ) as a function of frequency of NiO@C@PPy nanomaterial are due to NiO particle clustering in the polymer matrix [19]. The increased interfacial contacts between the polymer and NiO as a result of the order in these composites leads to maximum space charge (Maxwell Wagner) polarization. The fluctuation of dielectric loss for NiO@C@PPy nanomaterials with temperatures at various frequencies is shown in Fig. 7(c and d) at (183 K–328 K) & (333 K–363 K), respectively. Inset of Fig. 7(d) describes the activation energy of the NiO@C@PPy nanomaterial. Calculated as 0.32 eV. In the next section, EMI shielding of this material is performed, therefore, it will be worth noting that tangent loss at higher frequencies is lower than 1. This low tanδ value makes this material valuable for high-frequency applications.

Fig. 8(a and b) illustrates the log plot of conductivity against temperature for two distinct temperature ranges (183 K–328 K) & (333 K–363 K). These conductivity plots shows a frequency independent and dependent regions at lower and higher frequencies respectively. However, with temperature, the frequency at which frequency-independent conductivity transforms into frequency-dependent conductivity shifts in the direction of high frequency, implying the charge carriers hopping in the NiO@C@PPy nanomaterial [38]. Fig. 8(a and b) shows a clear change of conductivity trend at around 328 K, corresponding to SMT.

When conductivity is frequency-dependent it is governed by the equation $\sigma(\omega) = \sigma_0 + A\omega^s$ where "ω" denotes angular frequency (2πf), "σ(ω)" is the AC conductivity, "σ_0" is the DC conductivity, "s" is slope and "A" termed as pre-exponential factor [39]. The pre-exponential factor (A), which defines the degree of the polarizability, increases with rising temperature, the polarizability and consequently the dielectric characteristics also rise. The electrical conductivity of NiO@C@PPy nanomaterial has been measured as 4.5×10^{-4} S/cm. It might be a result of the efficient inclusion of NiO nanoparticles into the polymeric chain, which results in doping effects, drift in the electron density, and matrix expansion. As a consequence of the band alignment of NiO and PPy, the drift in electron
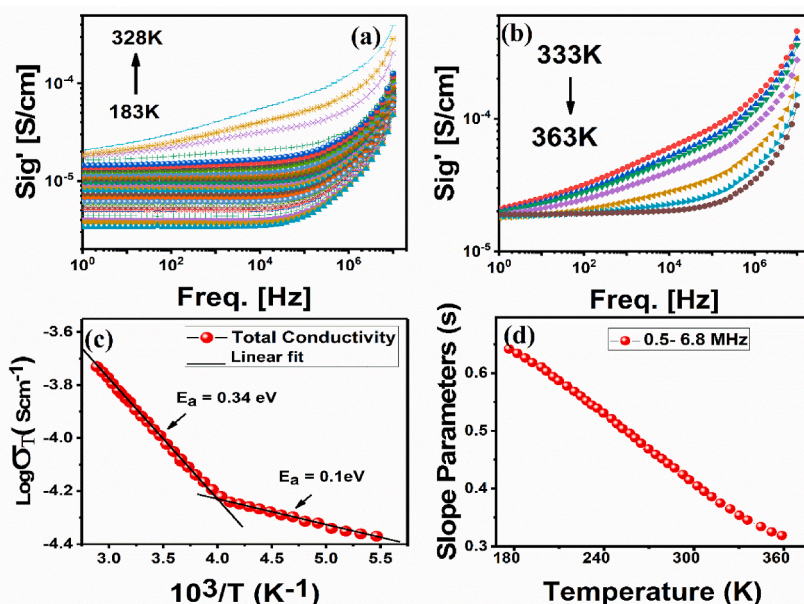

Fig. 8. (a–d) Variation of the AC conductivity of prepared multiphase NiO@C@PPy nanomaterial as a function of frequency at two different temperatures, (a) (183 K–328 K) & (b) (333 K–363 K). (c) Total conductivity of the multiphase NiO@C@PPy nanomaterial, the solid lines are the best fits the Arrhenius relation, and (d) variation of the slop parameters (s) at (183 K–363 K) temperatures at 0.5–6.8 MHz frequency range.

density also causes partial ionization to enhance electrical conductivity. It is also possible to interpret the change in electrical conductivity as an increase in PPy's d-spacing due to the composite's extended matrix. Due to the alignment of the structures in the composite, the interaction between NiO and PPy reduces the bandgap and forms a conducting channel for the electrons. A stronger connection has been achieved due to enhanced weak links between the polymer and the NiO particles. Pure polypyrrole is very light and has poor homogeneity due to the microparticles arbitrarily directed orientation and the weak interaction between the polymer particles.

Fig. 8(c) shows a conductivity plot at 10^7 Hz at different temperatures. Using the Arrhenius model, activation energy is calculated for two different segments. In the high-temperature region activation energy is calculated as 0.34 eV, which is in accordance with activation energies calculated from impedance and relaxation constants [40]. In the low-temperature region, E_a is calculated as 0.1 eV which is in accordance with E_a calculated from the SPH model in the same temperature range. From the high-frequency region, the slope is calculated which shows a change in the slope values that suggests the occurrence of a different conduction mechanism. With temperature, the relaxation time reduces linearly, at 248 K indicating a shift in the conduction mechanism. In the region of the space charge zone, carriers lacking sufficient energy to surpass the potential, expended the majority of their time at lower temperatures. The conduction mechanism of hopping carriers depend upon disorder and polarons which is related to the different levels of activation energies in accordance with relaxation processes [28]. These materials exhibit semiconducting or metallic properties when strong cation-anion-cation interactions prevail over weak cation-cation interactions [41]. We also conclude from the description above that the adiabatic SPH model in NiO nanograins may be responsible for the high dielectric constant. Fig. 8(d) shows a decreasing trend with temperature in the values of slope parameters. The closely packed anions that surround the cations may be regarded as being separated from one another because of the overlap of the charge clouds. This localization results in the formation of polarons. This leads to the conclusion that the ac conductivity in these multiphase NiO@C@PPy nanomaterials is carried out in such a way that the charge carriers follow the polaronic conduction mechanism which is temperature and frequency-dependent. In addition, the presence of defects further allows the charge transfer to occur between the closest neighbors [28].

In the X-band (8.2–12.4 GHz), VNA measured the total shielding efficiency based on scattering parameters S_{11}, S_{12}, S_{21} & S_{22} with the rectangular waveguide method. Shielding parameters of reflection (R), absorption coefficient (A) and transmittance (T) can be defined and related by equations (1)–(4) [42]:

$$R = |S_{11}|^2 = |S_{22}|^2 \tag{1}$$

$$T = |S_{12}|^2 = |S_{21}|^2 \tag{2}$$

$$T + R + A = 1 \tag{3}$$

$$A = 1 - R - T \tag{4}$$

The effective absorbance (A_{eff}), given below in equation (5), is the ratio of the absorption (A) with the effective power of incident EM wave inside the shielding material.
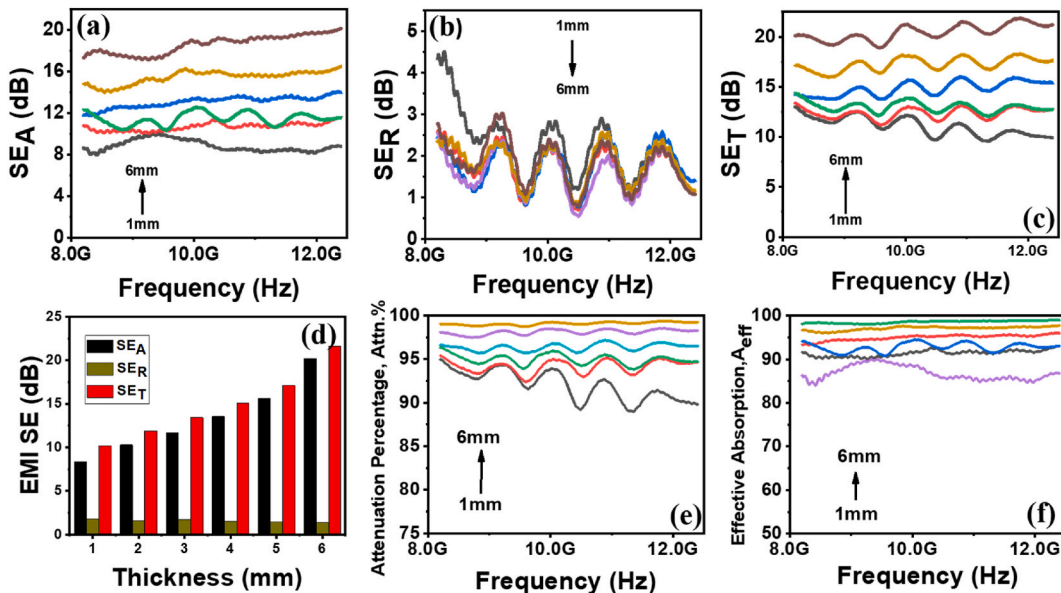

Fig. 9. (a–c) Depicts shielding parameters for absorption (SE$_A$), reflection (SE$_R$) & total SE (SE$_T$), respectively (d) SE$_A$, SE$_R$ and SE$_T$ against varying thicknesses (1 mm–6 mm) of the nanocomposite at 10.1 GHz, (e) shows the attenuation percentage & (f) shows the percentage of effective absorption.

$$A_{eff} = (1 - R - T) / (1 - R) \tag{5}$$

According to Schelkunoff's theory, total shielding effectiveness (SE_T) as defined in equation (6), where reflection shielding effectiveness is SE_R, absorption shielding effectiveness is SE_A and SE_{MR} is shielding effectiveness due to multiple reflections.

$$SE_T \ (dB) = SE_A + SE_R + SE_{MR} \tag{6}$$

For $SE_A \geq 10$ dB, SE_{MR} is generally discarded and the relationship reduces to equation (7):

$$SE_T \ (dB) = SE_A + SE_R \tag{7}$$

Considering the effective strength of the incoming electromagnetic wave inside the shielded material, the SE_R, SE_A, and SE_T from equation (7) may be stated in equations (8)–(10) [43].

$$SE_A = -10 \ log \ (1 - A_{eff}) \tag{8}$$

$$SE_R = -10 \ log \ (1 - R) \tag{9}$$

$$SE_T = -10 \ log T \tag{10}$$

Fig. 9(a) depicts the varied shielding effectiveness owing to the absorption characteristics within X-band range for varying thicknesses of NiO@C@PPy nanomaterials. The highest value of SE_A is $\approx$18 dB, whereas the SE_A decreases with the decrease in sample thickness. The NiO@C@PPy shows an absorption dominant EMI shielding mechanism which is desired for application in electronic industry related to EMI shielding products. Fig. 9(b) depicts the SE due to the reflection in the X-band with frequency for varying thicknesses of NiO@C@PPy nanomaterials. With increasing frequency, the shielding efficiency owing to reflection (SE_R) exhibits a constant trend as shielding effectiveness due to reflection mainly depends on the impedance match between the EMI shielding material and the electromagnetic wave propagation medium [43]. It can be infer that absorption is the main shielding mechanism of EM waves within the NiO@C@PPy nanomaterial. For all samples, SE_A is larger than SE_R in the overall comparison. The possible explanation for these mechanisms is due to the interesting microstructure of the system, which includes conductive (PPy, C), magnetic (Ni), and dielectric (NiO) loss mechanisms for EM waves. Fig. 9(c) shows the total shielding effectiveness (SE_T) for NiO@C@PPy nanomaterials. The conducting interconnected network formation between the conducting NiO and polymer matrix can be responsible for the rise in overall EMI in the nanomaterial respectively.

SE_T is around 13 dB (94% attenuation) for a sample with a thickness of 1 mm and it shows an increasing trend with the increase in thickness. The varying trend in SE_A, SE_R, and SE_T with thickness is displayed using a histogram for the data taken at a frequency of 10.2 GHz (Fig. 9(d)). Fig. 9(e and f) shows the variation of attenuation percentage and effective absorption percentage (A_{eff}) of NiO@C@PPy samples against frequency in the X-band. An attenuation percentage of 99.32, (see Table 2), is achieved and these results show exceptional shielding characteristics with an absorption dominant shielding mechanism.

4. Conclusions

NiO@C@PPy nanocomposite is synthesized by the combination of facile hydrothermal technique and in-situ chemical oxidative polymerization of the pyrrole monomers. The synthesis of NiO@C@PPy nanocomposite is facile, reproducible, and has a high yield. The structure and morphology is investigated by XRD and FE-SEM. The temperature-dependent conduction mechanism of electro-active regions present in the NiO@C@PPy nanocomposite is studied. NiO@C@PPy nanocomposite exhibits high dielectric constant characteristics with low tanδ values which can cater to the problem of leakage current.

Based on equivalent circuit model parameters, the SPH model is best fitted to explain the impedance and relaxation behavior of the material. The activation energy computed for the electroactive region is 0.32 eV. SMT behavior is observed around 328 K and a change in conduction mechanism is seen around SMT. A comparative analysis of impedance and modulus plots leads to the conclusion that below 328 K short-range carrier mobility is dominating, however, after and around SMT it changes to a long-range conduction mechanism. Finally, the as-prepared NiO@C@PPy showed excellent EMI shielding ability and absorption dominant electromagnetic shielding mechanism which is advantageous in critical applications. A maximum value of SE_T 21.9 dB in the X-band corresponding to different thicknesses value is achieved. In light of the above results, NiO@C@PPy is proposed as a promising candidate for EMI shielding along with SMT which can open new venues for fundamental studies and applications.

Statement and declaration

Data availability

Data associated with the study has not been deposited into any publicly available repository. Supporting data related to this manuscript will be available if required.

Table 2
Total shielding effectiveness compared with corresponding percentage attenuation for varying thicknesses of the NiO@C@PPy nanomaterial.

Sample Thickness (mm)	SE$_T$ (dB)	Attenuation percentage
1 mm	12.99	94.98
2 mm	13.37	95.40
3 mm	14.35	96.33
4 mm	15.84	97.13
5 mm	18.26	98.51
6 mm	21.96	99.32

CRediT authorship contribution statement

Ujala Anwar: Writing – review & editing, Writing – original draft, Methodology, Investigation. **Numrah Sultan:** Writing – review & editing, Writing – original draft, Software, Formal analysis. **Ghazala Yasmeen:** Writing – review & editing, Writing – original draft, Visualization, Supervision, Project administration. **Khaqan Shati:** Writing – review & editing, Writing – original draft. **M. Nadeem:** Writing – review & editing, Writing – original draft, Visualization, Validation, Supervision, Software, Resources, Project administration, Methodology, Investigation, Formal analysis, Data curation, Conceptualization.

Declaration of competing interest

The authors declare that they have no known competing financial interests or personal relationships that could have appeared to influence the work reported in this paper.

Acknowledgments

References

[1] Y. Cheng, W. Zhu, X. Lu, C. Wang, One-dimensional metallic, magnetic, and dielectric nanomaterials-based composites for electromagnetic wave interference shielding, Nano Res. 15 (2022) 9595–9613, https://doi.org/10.1007/s12274-022-4781-9.
[2] B. Dutta, E. Kar, G. Sen, N. Bose, S. Mukherjee, Lightweight, flexible NiO@SiO2/PVDF nanocomposite film for UV protection and EMI shielding application, Mater. Res. Bull. 124 (2020), 110746, https://doi.org/10.1016/j.materresbull.2019.110746.
[3] H.S. Ahmad, T. Hussain, Y. Nawab, S. Salamat, Effect of different dielectric and magnetic nanoparticles on the electrical, mechanical, and thermal properties of unidirectional carbon fiber-reinforced composites, Int. J. Polym. Sci. 2022 (2022), https://doi.org/10.1155/2022/5952450.
[4] Z. Li, et al., Nickel oxide film with tertiary hierarchical porous structure and high electrochromic performance and stability, Mater. Chem. Phys. 269 (March) (2021), https://doi.org/10.1016/j.matchemphys.2021.124738.
[5] Y. Liu, et al., Intense nonlinear dielectric and magnetic resonances of core-shell Ni@graphene composites and their improved microwave absorption properties, J. Mater. Chem. C 9 (14) (2021) 4910–4920, https://doi.org/10.1039/d0tc05946c.
[6] Y. Akaltun, T. Çayir, Fabrication and characterization of NiO thin films prepared by SILAR method, J. Alloys Compd. 625 (2015) 144–148, https://doi.org/10.1016/j.jallcom.2014.10.194.
[7] J. Cheng, et al., Construction of multiple interfaces and dielectric/magnetic heterostructures in electromagnetic wave absorbers with enhanced absorption performance: a review, J. Mater. 7 (6) (2021) 1233–1263, https://doi.org/10.1016/j.jmat.2021.02.017.
[8] F. Ren, Z.D. Huang, R. Ma, Q. Xie, Electronic structures, magnetic properties and dielectric properties of Fe3Si@SiO2 core-shell structure from first-principles study, Mater. Chem. Phys. 254 (May) (2020), 123282, https://doi.org/10.1016/j.matchemphys.2020.123282.
[9] L. Lei, et al., Hydrangea-like Ni/NiO/C composites derived from metal-organic frameworks with superior microwave absorption, Carbon N. Y. 173 (2021) 69–79, https://doi.org/10.1016/j.carbon.2020.10.093.
[10] X. Ma, K. lai Tang, M. Yang, W. Shi, W. Zhao, Metal–organic framework-derived yolk–shell hollow Ni/NiO@C microspheres for bifunctional non-enzymatic glucose and hydrogen peroxide biosensors, J. Mater. Sci. 56 (1) (2021) 442–456, https://doi.org/10.1007/s10853-020-05236-8.
[11] K. Manna, S.K. Srivastava, Fe3O4@Carbon@Polyaniline trilaminar core-shell composites as superior microwave absorber in shielding of electromagnetic pollution, ACS Sustain. Chem. Eng. 5 (11) (2017) 10710–10721, https://doi.org/10.1021/acssuschemeng.7b02682.
[12] X. Di, Y. Wang, Y. Fu, X. Wu, P. Wang, Wheat flour-derived nanoporous carbon@ZnFe2O4 hierarchical composite as an outstanding microwave absorber, Carbon N. Y. 173 (2021) 174–184, https://doi.org/10.1016/j.carbon.2020.11.006.
[13] L. Jiang, et al., Carbon-encapsulated fe nanoparticles embedded in organic polypyrrole polymer as a high performance microwave absorber, J. Phys. Chem. C 120 (49) (2016) 28320–28329, https://doi.org/10.1021/acs.jpcc.6b09445.
[14] P. Liu, Y. Huang, J. Yan, Y. Zhao, Magnetic graphene@PANI@porous TiO2 ternary composites for high-performance electromagnetic wave absorption, J. Mater. Chem. C 4 (26) (2016) 6362–6370, https://doi.org/10.1039/c6tc01718e.
[15] C. Zhang, Y. Chen, H. Li, R. Tian, H. Liu, Facile fabrication of three-dimensional lightweight RGO/PPy Nanotube/Fe3O4 aerogel with excellent electromagnetic wave absorption properties, ACS Omega 3 (5) (2018) 5735–5743, https://doi.org/10.1021/acsomega.8b00414.
[16] H. Gao, C. Wang, Z. Yang, Y. Zhang, 3D porous nickel metal foam/polyaniline heterostructure with excellent electromagnetic interference shielding capability and superior absorption based on pre-constructed macroscopic conductive framework, Compos. Sci. Technol. 213 (March) (2021), 108896, https://doi.org/10.1016/j.compscitech.2021.108896.
[17] K. Zhang, et al., Preparation and microwave absorption properties of carbon nanotubes/iron oxide/polypyrrole/carbon composites, Synth. Met. 260 (October) (2019), 116282, https://doi.org/10.1016/j.synthmet.2019.116282, 2020.
[18] M.A. Chougule, S.G. Pawar, P.R. Godse, R.N. Mulik, S. Sen, V.B. Patil, Synthesis and characterization of polypyrrole (PPy) thin films, Soft Nanosci. Lett. 1 (1) (2011) 6–10, https://doi.org/10.4236/snl.2011.11002.
[19] M. Kılıç, Natural additive material for desirable dielectric properties of polypyrrole: limestone, Synth. Met. 260 (July 2019) (2020), https://doi.org/10.1016/j.synthmet.2020.116297.

[20] C. Tian, et al., Constructing uniform core-shell PPy@PANI composites with tunable shell thickness toward enhancement in microwave absorption, ACS Appl. Mater. Interfaces 7 (36) (2015), https://doi.org/10.1021/acsami.5b05259, 20090–20099.

[21] F.M. Marsin, W.A. Wan Ibrahim, H.R. Nodeh, M.M. Sanagi, New magnetic oil palm fiber activated carbon-reinforced polypyrrole solid phase extraction combined with gas chromatography-electron capture detection for determination of organochlorine pesticides in water samples, J. Chromatogr. A 1612 (2020), 460638, https://doi.org/10.1016/j.chroma.2019.460638.

[22] Q. Wang, et al., Enhanced microwave absorption of biomass carbon/nickel/polypyrrole (C/Ni/PPy) ternary composites through the synergistic effects, J. Alloys Compd. 890 (2021), 161887, https://doi.org/10.1016/j.jallcom.2021.161887.

[23] A.S. Rajan, S. Sampath, A.K. Shukla, An in situ carbon-grafted alkaline iron electrode for iron-based accumulators, Energy Environ. Sci. 7 (3) (2014) 1110–1116, https://doi.org/10.1039/c3ee42783h.

[24] R. Strümpler, J. Glatz-Reichenbach, Conducting polymer composites, J. Electroceram. 3 (4) (1999) 329–346, https://doi.org/10.1023/A:1009909812823.

[25] P. Mallick, N.C. Mishra, Evolution of structure, microstructure, electrical and magnetic properties of nickel oxide (NiO) with transition metal ion doping, Am. J. Mater. Sci. 2 (3) (2012) 66–71, https://doi.org/10.5923/j.materials.20120203.06.

[26] R. Goel, R. Jha, C. Ravikant, Investigating the structural, electrochemical, and optical properties of p-type spherical nickel oxide (NiO) nanoparticles, J. Phys. Chem. Solid. 144 (November 2019) (2020) 109488, https://doi.org/10.1016/j.jpcs.2020.109488.

[27] S. Ahmed, et al., Enhancement in the magnetoelectric and energy storage properties of core-shell-like $CoFe_2O_4-BaTiO_3$ multiferroic nanocomposite, J. Alloys Compd. 883 (2021), 160875, https://doi.org/10.1016/j.jallcom.2021.160875.

[28] M. Younas, M. Atif, M. Nadeem, M. Siddique, M. Idrees, R. Grossinger, Colossal resistivity with diminished tangent loss in Zn-Ni ferrite nanoparticles, J. Phys. D Appl. Phys. 44 (2011) 34, https://doi.org/10.1088/0022-3727/44/34/345402.

[29] H. He, Metal Oxide Semiconductors and Conductors, Elsevier Inc., 2020, https://doi.org/10.1016/B978-0-12-814930-0.00002-5.

[30] D. Vanidha, A. Arunkumar, S. Rajagopan, R. Kannan, Semiconductor to metallic phase transition in nickel doped $Co_{0.5}Ni_X Fe_{(0.5-X)} Fe_2O_4$, J. Supercond. Nov. Magnetism 26 (1) (2013) 173–182, https://doi.org/10.1007/s10948-012-1705-z.

[31] Q. Zhao, et al., The discovery of conductive ionic bonds in NiO/Ni transparent counter electrodes for electrochromic smart windows with an ultra-long cycling life, Mater. Adv. 2 (14) (2021) 4667–4676, https://doi.org/10.1039/d1ma00384d.

[32] S.K. Hasanain, M. Nadeem, W.H. Shah, M.J. Akhtar, M.M. Hasan, Effects of iron doping on the transport and magnetic behaviour in $La_{0.65}Ca_{0.35}Mn_{1-y}FeyO_3$, J. Phys. Condens. Matter 12 (42) (2000) 9007–9017, https://doi.org/10.1088/0953-8984/12/42/307.

[33] S. Ahmed, M. Atif, M. Nadeem, Z. Ali, W. Khalid, M. Nasir Khan, Impedance spectroscopy and conduction mechanism of ferroelectric rich $PbZr_{0.52}Ti_{0.48}O_3-CoFe_2O_4$ magnetoelectric composite, Ceram. Int. 46 (13) (2020) 21090–21096, https://doi.org/10.1016/j.ceramint.2020.05.183.

[34] M. Atif, M. Nadeem, W. Khalid, Z. Ali, Structural, magnetic and impedance spectroscopy analysis of $(0.7)CoFe_2O_4+(0.3)BaTiO_3$ magnetoelectric composite, Mater. Res. Bull. 107 (May) (2018) 171–179, https://doi.org/10.1016/j.materresbull.2018.07.026.

[35] M. Radoičić, et al., Fine-tuning of conductive and dielectric properties of polypyrrole/TiO$_2$ nanocomposite-coated polyamide fabric, Compos. Interfac. 28 (8) (2021) 795–808, https://doi.org/10.1080/09276440.2020.1805219.

[36] R.A. Sutar, L. Kumari, M.V. Murugendrappa, Room temperature ac conductivity, dielectric properties and impedance analysis of polypyrrole-zinc cobalt oxide (PPy/ZCO) composites, Phys. B Condens. Matter 573 (July) (2019) 36–44, https://doi.org/10.1016/j.physb.2019.07.011.

[37] M. Musiani, M.E. Orazem, N. Pébère, B. Tribollet, V. Vivier, Constant-phase-element behavior caused by coupled resistivity and permittivity distributions in films, J. Electrochem. Soc. 158 (12) (2011) C424, https://doi.org/10.1149/2.039112jes.

[38] S. Ibadat, et al., Realistic dielectric response of high temperature sintered ZnO ceramic: a microscopic and spectroscopic approach, RSC Adv. 10 (51) (2020) 30451–30462, https://doi.org/10.1039/d0ra04273k.

[39] J. Bisquert, G. Garcia-Belmonte, Interpretation of AC conductivity of lightly doped conducting polymers in terms of hopping conduction, Russ. J. Electrochem. 40 (3) (2004) 352–358, https://doi.org/10.1023/B:RUEL.0000019676.99599.bc.

[40] A. Hakim, J. Hossain, K.A. Khan, Temperature effect on the electrical properties of undoped NiO thin films, Renew. Energy 34 (12) (2009) 2625–2629, https://doi.org/10.1016/j.renene.2009.05.014.

[41] M. Younas, M. Nadeem, M. Atif, R. Grossinger, Metal-semiconductor transition in NiFe$_2$O$_4$ nanoparticles due to reverse cationic distribution by impedance spectroscopy, J. Appl. Phys. 109 (2011) 9, https://doi.org/10.1063/1.3582142.

[42] M.S. Cao, W.L. Song, Z.L. Hou, B. Wen, J. Yuan, The effects of temperature and frequency on the dielectric properties, electromagnetic interference shielding and microwave-absorption of short carbon fiber/silica composites, Carbon N. Y. 48 (3) (2010) 788–796, https://doi.org/10.1016/j.carbon.2009.10.028.

[43] A. Raza, A. Nasir, M. Tahir, S. Taimur, T. Yasin, M. Nadeem, Synthesis and EMI shielding studies of polyaniline grafted conducting nanohybrid, J. Appl. Polym. Sci. 138 (2) (2021) 1–13, https://doi.org/10.1002/app.49680.